Chin. Phys. Lett. **39**, 026101 (2022)

First-Principles Calculations about Elastic and Li^+ Transport Properties of Lithium Superoxides under High Pressure and High Temperature

Yufeng Li(李玉峰)[1,2], Shichuan Sun(孙士川)[1,2], Yu He(何宇)[1,2,3*], and Heping Li(李和平)[1,2]

[1]*Key Laboratory of High-Temperature and High-Pressure Study of the Earth's Interior, Institute of Geochemistry, Chinese Academy of Sciences, Guiyang 550081, China*
[2]*University of Chinese Academy of Sciences, Beijing 100049, China*
[3]*Center for High Pressure Science and Technology Advanced Research, Shanghai 201203, China*

(Received 26 October 2021; accepted 29 December 2021; published online 29 January 2022)

Lithium superoxides, Li_2O_3, LiO_2, and LiO_4, have been synthesized under high pressure. These materials have potential applications in energy storage devices. Here, we use first-principles calculations to investigate the elastic and Li^+ transport properties of these oxides at high pressure and high temperature. The elastic constants are calculated at 20–80 GPa, and they satisfy the Born stability criteria, indicating the good mechanical stability of these oxides. Their sound velocities calculated with elastic constants are close to each other, but difference in velocity anisotropy is obvious. LiO_2 presents significant shear sound wave anisotropy over 80%. The Li^+ transport properties are investigated using first principles molecular dynamics (FPMD) and climbing-image nudged elastic band methods. The lowest Li^+ migration barrier energies increase from 0.93, 0.86 and 1.22 eV at 20 GPa to 1.43, 1.12 and 1.77 eV at 50 GPa for Li_2O_3, LiO_2, and LiO_4, respectively. The most favorable path for LiO_2 and LiO_4 is along the [001] direction. The FPMD results suggest that these oxides become unstable with increasing temperature up to 2000 K due to O–O dimer clusters in these superoxides. Consequently, a superionic transition is not observed in the simulations.

DOI: 10.1088/0256-307X/39/2/026101

Pressure is a basic thermodynamic variable that is able to tune the atomic distance and electronic structure of materials.[1,2] A large number of novel materials with distinctive properties, such as room-temperature superconductivity, are synthesized under high pressure.[3] Recently, superionic ice and hydrous minerals have been synthesized under high pressure and high temperature with great influence on the properties of Earth's and exoplanet interiors.[4,5]

High-pressure technology has also been used in the process of exploring novel materials for rechargeable batteries.[6−12] The electrode materials $LiMPO_4$ (M = Fe, Mn, Ni, CO) with olivine structure can change from olivine to $CrVO_4$ structures (β' phase) at high pressure and high temperature. Under higher pressure, the β' phase can transform into the spinel structure phase.[6,7] The transition from olivine structure to β' phase takes place at 6.5 GPa and 900 ℃. However, this transition does not improve electrochemical properties.[6] Wang *et al.* investigated the high-pressure structural change of layered $LiCoO_2$ using Raman spectroscopy and x-ray diffraction.[8] They found that an increase in pressure leads to a reduction in cell parameters with more significant compression of Li–O bonds. Thus, the c/a ratio decreases with increasing pressure. This trend continues without a phase transition at pressures below 26 GPa. Fell *et al.* treated $LiCoO_2$ under high pressure and high temperature, and found that pressure can indeed modify the crystal structure. However, the treatment reduces the electrochemical capacity of the material due to the confinement of Li^+ mobility.[9] Spinel $LiMn_2O_4$ changes from cubic to tetragonal structures at ∼0.1 GPa, and then changes to the $CaFe_2O_4$ structure at higher pressure.[10,11] Piszora *et al.* found that the phase transition at 0.1 GPa is mainly caused by the deformation of the $Mn^{3+}O_6$ octahedron under pressure, and the deformation of the $Mn^{3+}O_6$ octahedron leads to the enlargement of the lithium ion transmission channel. Therefore, they expect that this effect may improve the ionic conductivity of $LiMn_2O_4$.[11] Recently, Huang *et al.* observed an irreversible amorphous phase transition of spinel $Li_4Ti_5O_{12}$ (LTO) at ∼26.9 GPa.[12] The amorphous phase presents much higher conductivity than that of LTO at room temperature. The density functional theory (DFT) shows that the amorphous phase provides a low-barrier-energy migration path, which promotes Li^+ diffusion.

*Corresponding author. Email: heyu@mail.gyig.ac.cn
© 2022 Chinese Physical Society and IOP Publishing Ltd

Previous high-pressure studies mostly focus on the structural evolution of widely used materials. Currently, high pressure has become an important method for exploring completely new materials.[13] Recently, several lithium superoxides, Li_2O_3, LiO_2, and LiO_4, have been synthesized under high pressure.[13] These novel lithium oxides show great potential in improving battery design and performance in large battery applications under extreme conditions.[13] Therefore, it is necessary to study various properties of these Li–O compounds under extreme conditions such as high pressure. In these oxides, Li atoms are dispersed into dimer O–O frameworks, which is similar to the high-pressure oxygen phase ε-O_8.[14,15] The electronic structures of these oxides have been studied before.[16] However, the mechanical and thermal stability of these oxides is still unknown. In particular, whether a superionic transition can take place in these lithium oxides is important for material design of lithium ion batteries at high pressure.

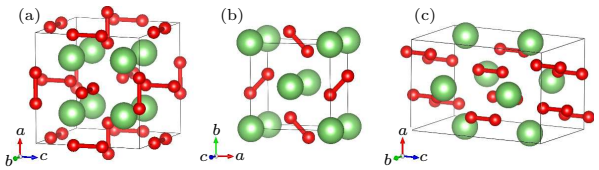

Fig. 1. Crystal structures of three lithium oxide phases. The atomic structure arrangements in the unit cell: (a) high pressure Li_2O_3, (b) high pressure LiO_2, and (c) high pressure LiO_4. Red and green spheres represent oxygen and lithium atoms, respectively. Red sticks indicate the O–O bands.

Lithium superoxides Li_2O_3 ($Im\bar{3}m$), LiO_2 ($P4/mbm$), and LiO_4 ($Ibam$) have been proven to be stable at high pressure based on the combination of experimental and computational methods.[13] The structures of these oxides are shown in Fig. 1, and the increase in oxygen content leads to a decrease in the distance between two oxygen atoms in the O–O dimer cluster. The DFT has proven to be a powerful tool for studying the structure and thermodynamics of various materials at high pressure.[17] The Vienna *ab initio* simulation package (VASP) based on the DFT was used to calculate the properties of these oxides.[18–20] The DFT calculations were conducted within the Perdew–Burke–Ernzerhof (PBE)[21] functional in the projected augmented wave (PAW) method. A plane-wave energy cutoff of 650 eV was used in the calculations, and a k-point mesh with a spacing of about 0.04 $Å^{-1}$ was adopted.[22] Geometry optimizations were performed by using conjugate gradient minimization until all the forces acting on ions were less than 0.01 eV/Å per atom.[22] Yang *et al.* found that these three oxides are stable at 50 GPa by calculation based on the DFT. Therefore, we first relaxed the structures at 50 GPa and then changed the cell volumes to calculate the cell parameters at different volumes. The calculated densities and cell parameters at different pressures (20–80 GPa) are shown in Fig. 2(a) and Fig. S1. The cell densities increase with pressure and oxygen content. As shown in Fig. S1, the reduction in the cell parameters of LiO_2 and LiO_4 with increasing pressure is anisotropic. The c-axis of LiO_2 and ab-plane of LiO_4 are more compressible than other directions.

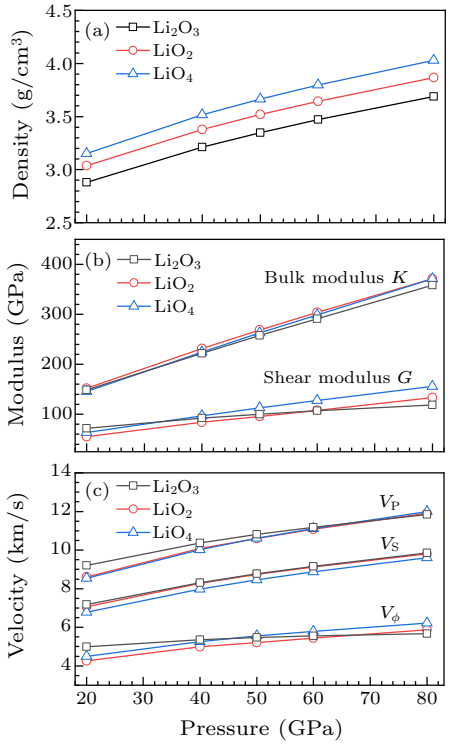

Fig. 2. Variation in density (a), modulus (b) and velocity (c) with pressure. The black lines and squares are for Li_2O_3, the red lines and circles for LiO_2, the blue lines and triangles for LiO_4.

The elastic constants of these superoxides at various pressures (Table 1) were calculated by solving the stress–strain relations (the detailed method is provided in the Supplementary Material). The stability of these superoxides was justified using the Born stability criteria.[23] For a cubic crystal system (Li_2O_3, $Im\bar{3}m$) with only 3 independent constants, the Born stability criteria[23] are defined as

$$C_{11} - C_{12} > 0, \quad C_{11} + 2C_{12} > 0, \quad C_{44} > 0. \tag{1}$$

For tetragonal classes (LiO_2, $P4/mbm$) with 6 independent elastic constants, the necessary and sufficient conditions[23] can be expressed as follows:

$$C_{11} > |C_{12}|, \quad 2C_{13}^2 < C_{33}(C_{11} + C_{12}),$$
$$C_{44} > 0, \quad C_{66} > 0. \tag{2}$$

For orthorhombic systems (LiO_4, $Ibam$) with 9 constants and no relationships between them, the

Born criteria[23] are known as

$$\begin{aligned} &C_{11} > 0; \quad C_{11}C_{22} > C_{12}^2, \\ &C_{11}C_{22}C_{33} + 2C_{12}C_{13}C_{23} - C_{11}C_{23}^2, \\ &- C_{22}C_{13}^2 - C_{33}C_{12}^2 > 0, \\ &C_{44} > 0, \quad C_{55} > 0, \quad C_{66} > 0. \end{aligned} \tag{3}$$

The calculated elastic constants satisfied the Born stability criteria, indicating the good mechanical stability of these phases at pressures from 20 to 80 GPa. Moreover, we calculated the bulk and shear modulus using the calculated elastic constants. The Voigt–Reuss–Hill averaging scheme[24–26] was used to estimate the elastic moduli. The Hill averaging of bulk and shear moduli [Fig. 2(b)] are defined as

$$B = \frac{B_{\rm V} + B_{\rm R}}{2}, \quad G = \frac{G_{\rm V} + G_{\rm R}}{2}, \tag{4}$$

where $B_{\rm V}$ and $G_{\rm V}$ represent the Voigt approximation,[24] $B_{\rm R}$ and $G_{\rm R}$ indicate the Reuss approximation.[25] For the Voigt approximation, these moduli can be expressed as the calculated elastic constants:

$$B_{\rm V} = \frac{C_{11} + C_{22} + C_{33} + 2(C_{12} + C_{13} + C_{23})}{9}, \tag{5}$$

$$\begin{aligned} G_{\rm V} = &[C_{11} + C_{22} + C_{33} - (C_{12} + C_{13} + C_{23}) \\ &+ 3(C_{44} + C_{55} + C_{66})]/15. \end{aligned} \tag{6}$$

For the Reuss approximation, these moduli can be expressed as the calculated elastic constants:

$$B_{\rm R} = \frac{1}{S_{11} + S_{22} + S_{33} + 2(S_{12} + S_{13} + S_{23})}, \tag{7}$$

$$\begin{aligned} G_{\rm R} = &15/[4(S_{11} + S_{22} + S_{33}) - 4(S_{12} + S_{13} + S_{23}) \\ &+ 3(S_{44} + S_{55} + S_{66})]. \end{aligned} \tag{8}$$

Here, S_{ij} represents the elastic compliance, which is the inverse of C_{ij}. The calculated moduli were used to determine the sound velocities, including compressional wave velocity $V_{\rm P}$, shear wave velocity $V_{\rm S}$ and bulk sound velocity V_φ [Fig. 2(c)],

$$V_{\rm P} = \sqrt{\frac{B + \frac{4G}{3}}{\rho}}, \quad V_{\rm S} = \sqrt{\frac{G}{\rho}}, \quad V_\varphi = \sqrt{\frac{B}{\rho}}. \tag{9}$$

To calculate the elastic anisotropy, we solved the Christoffel equation[27,28] to obtain the sound velocities in different directions:

$$|C_{ijkl}n_j n_l - \rho V^2 \delta_{ik}| = 0, \tag{10}$$

where n_i and n_j are the propagation direction, ρ is the density, V is the velocity, and δ_{ik} is the Kroenecker delta function. The calculated velocities in different directions were used to obtain the anisotropy (more detail can be found in the Supplementary Material). The anisotropies of the p- and s-waves are defined as

$$AV = \frac{(V^{\rm MAX} - V^{\rm MIN})}{(V^{\rm MAX} + V^{\rm MIN})} \times 200, \tag{11}$$

where $V^{\rm MAX}$ and $V^{\rm MIN}$ are the maximum and minimum velocities, respectively. The velocities along lattice directions are exhibited by circular patterns (Fig. 3). Although the sound velocities in the three oxides are quite close at 20–80 GPa, the velocity anisotropy patterns are quite different (Fig. 3 and Fig. S2). In particular, LiO_2 presents significant velocity anisotropy with the anisotropy of $V_{\rm S}$ reaching 83%, which will lead to significant sound wave splitting in this material.

Table 1. The elastic constants and wave velocities of Li_2O_3, LiO_2, and LiO_4 at 20–80 GPa.

Crystal	P (GPa)	C_{11}	C_{22}	C_{33}	C_{44}	C_{55}	C_{66}	C_{12}	C_{13}	C_{23}	ρ (g/cm^3)	$V_{\rm P}$ (km/s)	$V_{\rm S}$ (km/s)	V_φ (km/s)
LiO_2	20	264.4		267.2	17.9		170	143	72.7		3.04	8.61	4.25	7.07
	40	385.8		406.3	34.1		223.9	204.8	124.5		3.38	10.08	4.99	8.27
	50	443.2		465.1	39.1		251.5	232.4	150.7		3.52	10.61	5.21	8.73
	60	500.8		520.4	46.4		267.8	259.9	173.6		3.64	11.08	5.44	9.13
	80	615.9		627.2	58.7		325.3	316.2	213.7		3.87	11.91	5.87	9.80
		C_{11}	C_{22}	C_{33}	C_{44}	C_{55}	C_{66}	C_{12}	C_{13}	C_{23}				
LiO_4	20	232.5	233.4	309.4	51.4	51.8	64.7	139.8	63.2	63.4	3.15	8.54	4.49	6.79
	40	352.3	350.9	468.2	81.2	81.3	97.8	207.8	106.6	109.2	3.52	10.20	5.25	7.98
	50	407.8	406.1	556.7	93.8	95.2	113.8	240.1	127.1	130.2	3.67	10.61	5.55	8.47
	60	462.6	462.8	614.9	107.9	107.9	129.1	269.9	152.2	151.9	3.80	11.11	5.79	8.86
	80	566.9	566.6	759.8	132.5	132.6	158.6	328.5	198.7	198.8	4.03	11.99	6.22	9.60
		C_{11}			C_{44}			C_{12}						
Li_2O_3	20	228.1			80.9			109			2.88	9.21	4.98	7.18
	40	308.1			116.7			178.7			3.21	10.36	5.36	8.31
	50	345.1			133.2			213.7			3.35	10.81	5.47	8.77
	60	379			147.8			246.8			3.47	11.18	5.55	9.16
	80	445.9			176.2			314.7			3.69	11.84	5.67	9.86

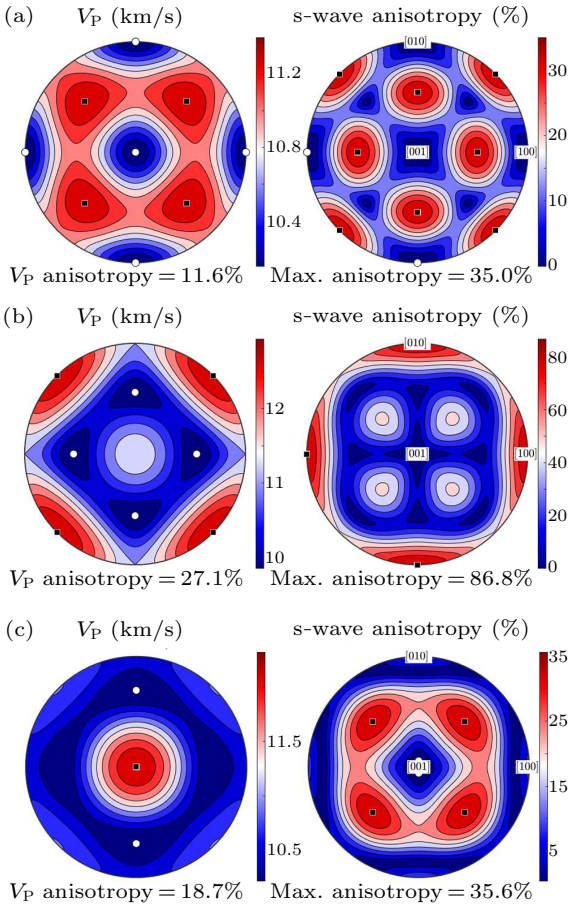

Fig. 3. The sound velocity anisotropy in Li_2O_3 (a), LiO_2 (b) and LiO_4 (c) at 50 GPa. The black squares mark the maximum, and the white circles mark the minimum.[29]

Lithium oxides have been widely studied for applications in lithium-ion batteries. Thus, Li^+ transportation properties are important for novel lithium superoxides. Li migration barrier energies along different directions were calculated by the climbing-image nudged elastic band (CINEB) method[30] at 20 and 50 GPa. Larger supercells adopted for the calculations were made up of $2\times2\times2$, $2\times2\times4$ and $2\times2\times2$ containing 160, 96 and 160 atoms for Li_2O_3, LiO_2 and LiO_4, respectively (see the Supplementary Material). The Li^+ migration energy in Li_2O_3 is isotropic, and the barrier energy is 0.93 eV at 20 GPa and increases to 1.43 eV at 50 GPa. For LiO_2 and LiO_4, Li^+ migration is anisotropic, and the most favorable path is along the [001] direction. The Li^+ migration barrier energy of LiO_2 along the [001] is 0.86 eV at 20 GPa, and other Li^+ migration barrier energies in these superoxides exceed 1.0 eV, which is much higher than that in antifluorite Li_2O at the same pressure.[22] Li^+ diffusion in Li_2O is isotropic, which benefits Li^+ transportation. Moreover, all Li^+ migration barrier energies are markedly increased with pressure (Fig. 4). This is consistent with the barrier energy change in Li_2O.[22] This suggests that these superoxides may not be favorable for Li^+ diffusion and that high pressure further inhibits diffusion.

First-principles molecular dynamics (FPMD) was used to investigate the Li^+ diffusion and stability of LiO_2, LiO_4 and Li_2O_3 under high pressure and temperature.[31] An equilibration step was carried out in the NPT ensemble (constant N, P, T) using a Langevin thermostat.[32–34] Larger supercells, $2\times2\times2$ for Li_2O_3, $2\times2\times4$ for LiO_2, and $2\times2\times1$ for LiO_4, were used for the FPMD simulations, and the simulations were conducted at hydrostatic 50 GPa and at temperatures from 1000 to 3000 K with a time step of 1 fs lasting over 14000 steps.[22,35]

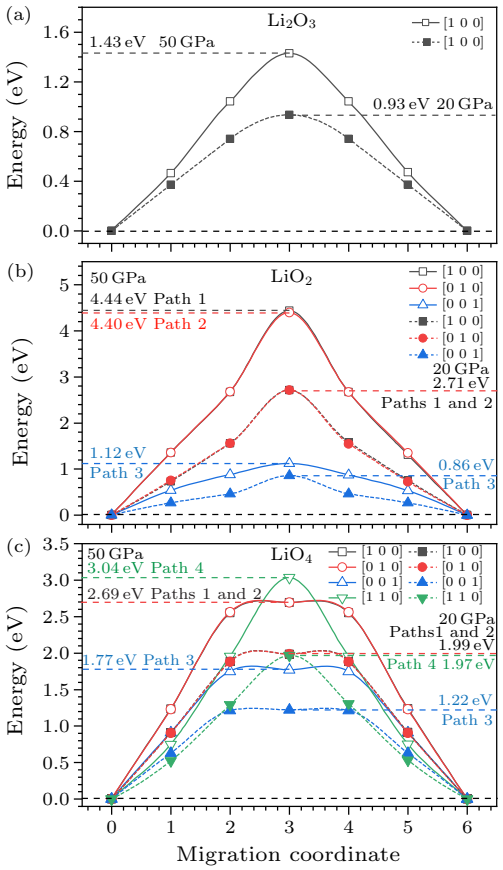

Fig. 4. Migration paths and related barrier energies for Li^+ in Li–O compounds at 20 and 50 GPa. (a) Calculated barrier energies for Li^+ migration along the [100] direction in Li_2O_3. (b) Calculated barrier energies for Li^+ migration along the [100], [010], and [001] directions in LiO_2. (c) Calculated barrier energies for Li^+ migration along the [100], [010], [001] and [110] directions in LiO_4. The results at 20 and 50 GPa are represented with dashed lines and solid lines, respectively. The migration paths are represented with color spheres in Fig. S4.

The mean square displacements (MSDs) are calculated at different temperatures using

$$\langle[\boldsymbol{r}(t)]^2\rangle = \frac{1}{N}\sum_{i=1}^{N}\langle[\boldsymbol{r}_i(t+t_0)-\boldsymbol{r}_i(t_0)]^2\rangle. \qquad (12)$$

Here, $\boldsymbol{r}_i(t)$ is the displacement of the Li^+ or O^{2-} at time t, and N is the total number of Li^+ or O^{2-} ions in the system. The increase in MSD with simulation time

denotes the diffusion of Li^+ or O^{2-} indicting the instability of the oxide. As shown in Fig. 5, both Li^+ and O^{2-} in these three oxides start to diffuse at 2000 K, 1300 K, and 2100 K for Li_2O_3, LiO_2 and LiO_4, respectively. In agreement with the previous quasiharmonic approximation (QHA) calculations,[13] LiO_2 shows a tendency to become less stable at temperatures above 1000 K. Our simulations suggest that the instability of LiO_2 is caused by the diffusion of oxygen. Li_2O_3 is a metastable phase presenting and is less stable than LiO_4. Other than O–O dimer clusters, single O atoms and larger clusters containing 3 or 4 oxygen atoms are observed in the structures after FPMD simulations (Fig. 6). This suggests that the oxygen dimer (O–O) cluster is unstable at high temperature. The instability of the O–O cluster can also be observed in the radial distribution function (Fig. S3). The stabilization of O–O clusters at high pressure promotes the formation of these lithium superoxides. However, the O–O cluster presents weak thermal stability at temperatures over 2000 K, which prevents the superionic transition in these superoxides.

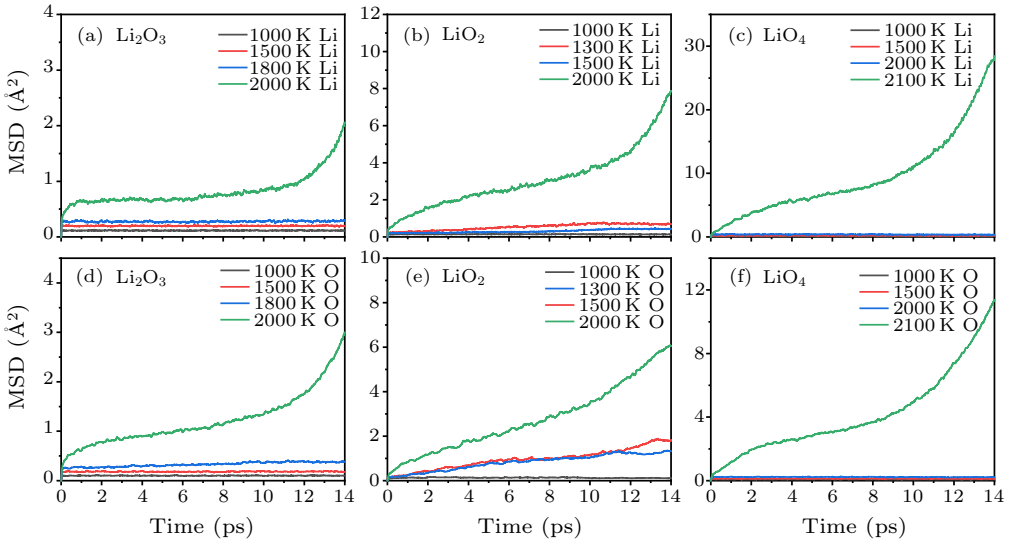

Fig. 5. Calculated mean square displacements at 50 GPa and temperatures from 1000–3000 K. MSD of Li in (a) Li_2O_3, (b) LiO_2 and (c) LiO_4; MSD of O in (d) Li_2O_3, (e) LiO_2, and (f) LiO_4.

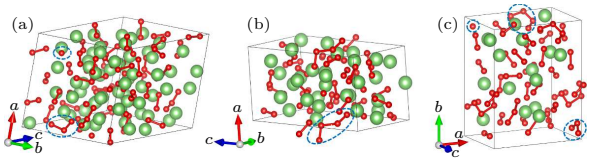

Fig. 6. Structures of Li_2O_3, LiO_2 and LiO_4 at 50 GPa and at different temperatures after the FPMD simulations. (a) Li_2O_3, 2000 K, (b) LiO_2, 2000 K, (c) LiO_4, 2500 K. The different O–O bands included in blue dashed circles indicate different O–O interactions at high pressure and temperature.

In summary, the elastic properties and ionic transport properties of Li_2O_3, LiO_2 and LiO_4 are studied using first-principles calculations. The elastic constants of these oxides satisfy the Born criteria and are mechanically stable at 20–80 GPa. The sound velocities in these oxides are similar, but LiO_2 presents anomalously high sound velocity anisotropy. The Li^+ migration barrier energy is over 1.0 eV at 50 GPa and increases with pressure. These oxides become unstable at temperatures above 2000 K due to the instability of the O–O cluster, which hinders the superionic transition in these superoxides.

Acknowledgments. This work was supported by the Strategic Priority Research Program (B) of the Chinese Academy of Sciences (Grant No. XDB18010401), the National Natural Science Foundation of China (Grant Nos. 42074104, 41774101, and 11974112), and the Youth Innovation Promotion Association of CAS (Grant No. 2020394).

References

[1] Badding J V 1998 *Annu. Rev. Mater. Sci.* **28** 631
[2] Paul F and M 2002 *Nat. Mater.* **1** 19
[3] Snider E, Dasenbrock-Gammon N, McBride R, Debessai M, Vindana H, Vencatasamy K, Lawler K V, Salamat A and Dias P 2020 *Nature* **586** 373
[4] Millot M and Coppari F 2019 *Nature* **569** 251
[5] Hou M Q, He Y, Jang B G, Sun S C, Zhuang Y K, Deng L W, Tang R L, Chen J H, Ke F, Meng Y, Prakapenka V B, Chen B, Shim J H, Liu J, Kim D Y, Hu Q Y, Pickard C J, Needs R J and Mao H K 2021 *Nat. Geosci.* **14** 174
[6] García-Moreno O, Alvarez-Vega M, García-Alvarado F, García-Jaca J, Gallardo-Amores J M, Sanjuán M L and Amador U 2001 *Chem. Mater.* **13** 1570
[7] Amador U, Gallardo-Amores J M, Heymann G, Huppertz H, Morán E and Arroyo-de Dompablo M E 2009 *Solid State Sci.* **11** 343
[8] Wang X, Loa I, Kunc K, Syassen K and Amboage M 2005 *Phys. Rev. B* **72** 224102
[9] Fell C R, Lee D H, Meng Y S, Gallardo-Amores J M, Moran E and Arroyo-de Dompablo M E 2012 *Energy Environ. Sci.*

5 6214
[10] Piszora P, Nowicki W and Darul J 2008 *J. Mater. Chem.* **18** 2447
[11] Yamaura K, Huang Q Z, Zhang L Q, Takada K, Baba Y, Nagai T, Matsui Y, Kosuda K and Takayama-Muromachi E 2006 *J. Am. Chem. Soc.* **128** 9448
[12] Huang Y W, He Y, Sheng H, Lu X, Dong H N, Samanta S, Dong H L, Li X F, Kim D Y, Mao H K, Liu Y Z, Li H P, Li H and Wang L 2019 *Natl. Sci. Rev.* **6** 239
[13] Yang W G, Kim D Y, Yang L X, Li N N, Tang L Y, Amine K and Mao H K 2017 *Adv. Sci.* **4** 1600453
[14] Lundegaard L F, Weck G, Mcmahon M I, Desgreniers S and Loubeyre P 2006 *Nature* **443** 201
[15] Meng Y, Eng P J, Tse J S, Shaw D M, Hu M Y, Shu J, Gramsch S A, Kao C, Hemley R J and Mao H K 2008 *Proc. Natl. Acad. Sci. USA* **105** 11640
[16] Dong X, Hou J Y, Kong J, Cui H X, Li Y L, Oganov A R, Li K, Zheng H Y, Zhou X F and Wang H T 2019 *Phys. Rev. B* **100** 144104
[17] Stixrude L, Cohen R E and Hemley R J 1998 *Rev. Mineral. Geochem.* **37** 639
[18] Kresse G 1995 *J. Non-Cryst. Solids* **192** 222
[19] Kresse G and Furthmüller J 1996 *Phys. Rev. B* **54** 11169
[20] Kresse G and Furthmüller J 1996 *Comput. Mater. Sci.* **6** 15
[21] Perdew J and Zunger A 1981 *Phys. Rev. B* **23** 5048
[22] He Y, Sun S and Li H P 2021 *Phys. Rev. B* **103** 174105
[23] Mouhat F and Coudert F X 2014 *Phys. Rev.* **90** 224104
[24] Voigt W 1928 *Lehrbuch der Kristallphysik* (Leipzig: Teubner) (in Germany)
[25] Reuss A 1929 *Z. Angew. Math. Mech.* **9** 49
[26] Hill B R 1952 *Proc. Phys. Soc. Sect. A* **65** 349
[27] Anderson D 1989 *Theory of the Earth* (Boston: Blackwell Scientific)
[28] Karki B B, Stixrude L, Clark S J, Warren M C, Ackland G J and Crain J 1997 *Am. Mineral.* **82** 51
[29] Mainprice D, Hielscher R and Schaeben H 2011 *Geological Society London Special Publications* **360** 175
[30] Henkelman G B, Uberuaga P and Jónsson H 2000 *J. Chem. Phys.* **113** 9901
[31] Bühl M and Kabrede H 2006 *ChemPhysChem.* **7** 2290
[32] Allen M P and Tildesley D J 1991 *Computer Simulation of Liquids* (New York: Oxford University Press)
[33] Parrinello M and Rahman A 1980 *Phys. Rev. Lett.* **45** 1196
[34] Parrinello N and Rahman A 1981 *J. Appl. Phys.* **52** 7182
[35] Sun S C and He Y 2019 *Phys. Chem. Miner.* **46** 935

Supplementary material for "First-principles investigation of the elastic and Li^+ transport properties of lithium superoxides under high pressure and temperature"

Yufeng Li(李玉峰)[1,2], Shichuan Sun(孙士川)[1,2], Yu He(何宇)[1,2,3*], and Heping Li(李和平)[1,2],

[1]Key Laboratory of High-Temperature and High-Pressure Study of the Earth's Interior, Institute of Geochemistry, Chinese Academy of Sciences, Guiyang 550081, Guizhou, China

[2]University of Chinese Academy of Sciences, Beijing 100049, China

[3]Center for High Pressure Science and Technology Advanced Research, Shanghai 201203, China

*E-mail: heyu@mail.gyig.ac.cn

DETAILS ON COMPUTATIONAL METHODS

The elastic constants calculation

The elastic constants of the crystal are expressed as the relationship between stress σ and strain ε:

$$\sigma_{ij} = C_{ijkl}\,\varepsilon_{kl} \#(1)$$

where σ_{ij} is the stress tensor, ε_{kl} refers to the strain tensor, and C_{ijkl} is the elastic modulus which is a fourth-order tensor. Furthermore, we determined the independent elastic constants according to different crystal systems, which contributes to reducing the computation. Considering the symmetry of C_{ijkl}, the equation can be simplified as follows:

$$\sigma_i = C_{ij}\,\varepsilon_j \#(2)$$

The equation could be expanded as follow:

$$\begin{pmatrix}\sigma_1\\ \sigma_2\\ \sigma_3\\ \sigma_4\\ \sigma_5\\ \sigma_6\end{pmatrix} = \begin{pmatrix} C_{11} & C_{12} & C_{13} & C_{14} & C_{15} & C_{16}\\ & C_{22} & C_{23} & C_{24} & C_{25} & C_{26}\\ & & C_{33} & C_{34} & C_{35} & C_{36}\\ & & & C_{44} & C_{45} & C_{46}\\ & & & & C_{55} & C_{56}\\ & & & & & C_{66}\end{pmatrix} \times \begin{pmatrix}\varepsilon_1\\ \varepsilon_2\\ \varepsilon_3\\ \varepsilon_4\\ \varepsilon_5\\ \varepsilon_6\end{pmatrix} \#(3)$$

where ε_j $(j = 1, \cdots, 6)$ corresponds to the following equation:

$$\varepsilon = \begin{pmatrix}\varepsilon_1 & \varepsilon_6 & \varepsilon_5\\ \varepsilon_6 & \varepsilon_2 & \varepsilon_4\\ \varepsilon_5 & \varepsilon_4 & \varepsilon_3\end{pmatrix} \#(4)$$

For a cubic crystal system (Li_2O_3, $I\,m\bar{3}m$) with only 3 independent constants, C_{11}, C_{12}, and C_{44}, we can calculate C_{11}, C_{12} by a strain tensor:

$$\varepsilon = \begin{pmatrix}\delta & 0 & 0\\ 0 & 0 & 0\\ 0 & 0 & 0\end{pmatrix} \#(5)$$

and we obtained C_{44} using a strain tensor as below:

$$\varepsilon = \begin{pmatrix} 0 & 0 & 0 \\ 0 & 0 & \delta/2 \\ 0 & \delta/2 & 0 \end{pmatrix} \#(6)$$

where δ is the magnitude of deformation. To reduce the error and obtain more accurate results, we exerted the strain symmetrically for ε_4 , ε_5 and ε_6.

For tetragonal classes $(4/mmm)$ (LiO_2, $P\,4/mbm$) with 6 independent elastic constants, $C_{11}, C_{33}, C_{44}, C_{66}, C_{12}, C_{13}$, we can calculate C_{11}, C_{12}, C_{13} by a strain tensor as Eq. (5) and calculate C_{33} by a strain tensor as follows:

$$\varepsilon = \begin{pmatrix} 0 & 0 & 0 \\ 0 & 0 & 0 \\ 0 & 0 & \delta \end{pmatrix} \#(7)$$

Moreover, we obtained C_{44} using a strain tensor:

$$\varepsilon = \begin{pmatrix} 0 & 0 & 0 \\ 0 & 0 & \delta/2 \\ 0 & \delta/2 & 0 \end{pmatrix} \#(8)$$

and obtained C_{66} using a strain tensor:

$$\varepsilon = \begin{pmatrix} 0 & \delta/2 & 0 \\ \delta/2 & 0 & 0 \\ 0 & 0 & 0 \end{pmatrix} \#(9)$$

For orthorhombic systems (LiO_4, $I\,bam$) with 9 constants and no relationships between them, $C_{11}, C_{22}, C_{33}, C_{44}, C_{55}, C_{66}, C_{12}, C_{13}, C_{23}$, we can calculate C_{11}, C_{12}, C_{13} by a strain tensor as Eq.(5) and calculate C_{22}, C_{23} using a strain tensor:

$$\varepsilon = \begin{pmatrix} 0 & 0 & 0 \\ 0 & \delta & 0 \\ 0 & 0 & 0 \end{pmatrix} \#(10)$$

We can also calculate C_{33}, C_{44}, C_{66} by a strain tensor as Eq. (7), (8) and (9), respectively. In addition, we calculated C_{55} by a strain tensor as follows:

$$\varepsilon = \begin{pmatrix} 0 & 0 & \delta/2 \\ 0 & 0 & 0 \\ \delta/2 & 0 & 0 \end{pmatrix} \#(11)$$

With those structures at different pressures, we exerted positive and negative strains $\Delta\varepsilon$ in $\pm 0.01, \pm 0.005, 0$ on them in each direction to accurately determine the stresses in the appropriate limit of zero strain. The relation between the strained lattice matrix a' and the unstrained lattice matrix a is defined by:

$$a' = a(I + \varepsilon) \#(12)$$

where I represents third-order identity matrix. The elastic constants are determined by the stress – strain:

$$\Delta\sigma = C_{ij} \cdot \Delta\varepsilon \#(13)$$

where C_{ij} is the elastic constant, $\Delta\varepsilon$ is the exerted strain and $\Delta\sigma$ is the stress caused by $\Delta\varepsilon$.

The elastic anisotropy

In high-symmetry directions, when polarization directions are parallel or vertical with the propagation directions of velocities, the modes are called pure longitudinal or transverse,

respectively. In general directions, the velocities are divided into quasi-longitudinal V_P (closest to propagation directions) and two spitting shear-wave velocities (V_{S1} and V_{S2}). The seismic anisotropy of the P wave and S wave are defined as:

$$AV = \frac{(V^{MAX} - V^{MIN})}{(V^{MAX} + V^{MIN})} \times 200\#(14)$$

where V^{MAX} and V^{MIN} are the maximum and minimum velocities, respectively. The velocities along lattice directions are exhibited by circular patterns (Fig. 3).

The migration barrier energy calculations

The Li^+ migration barrier energy was calculated by the climbing-image nudged elastic band (CINEB) method. Larger supercells adopted for the calculations were made up of 2×2×2, 3×3×4 and 2×2×2 containing 160, 96 and 160 atoms for Li_2O_3, LiO_2 and LiO_4, respectively. Five images were duplicated in our simulations between the starting point and the end point of migration ions to simulate the intermediate states. For the large supercell adopted in the CINEB calculations, only the gamma point was adopted for k-point sampling to reduce the computational cost. The convergence check indicated that a denser k mesh did not affect our conclusion.

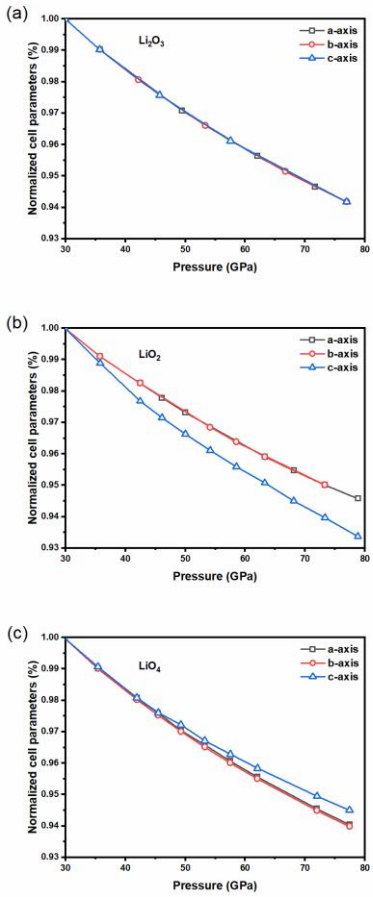

Fig. S1 The pressure dependence of normalized cell parameters to the values at 30 GPa. (a) Li_2O_3, (b) LiO_2, (c) LiO_4.

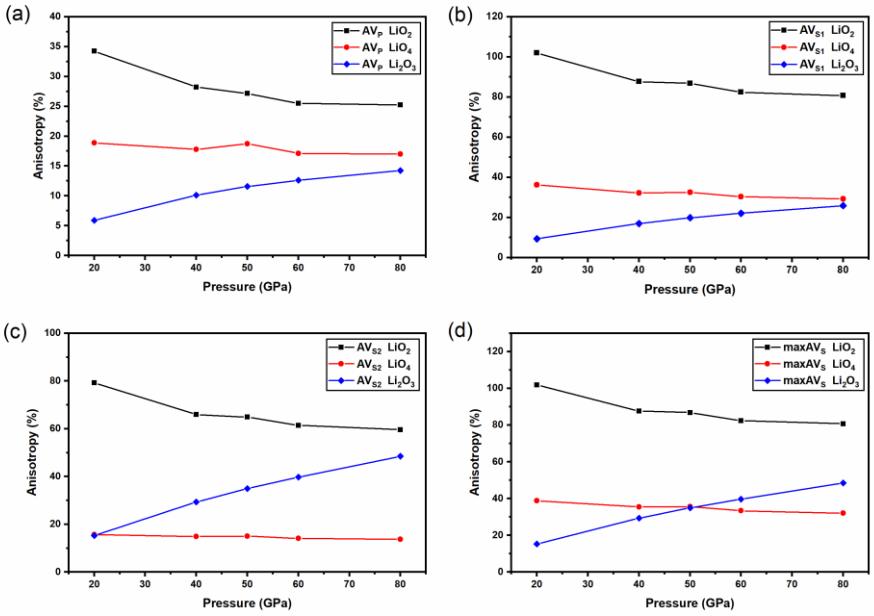

Fig. S2 The evolution of seismic velocity anisotropies with pressure. (a) P-wave anisotropy. (b) Anisotropy of fast S-wave velocities. (c) Anisotropy of slow S-wave velocities. (d) The max AV_S.

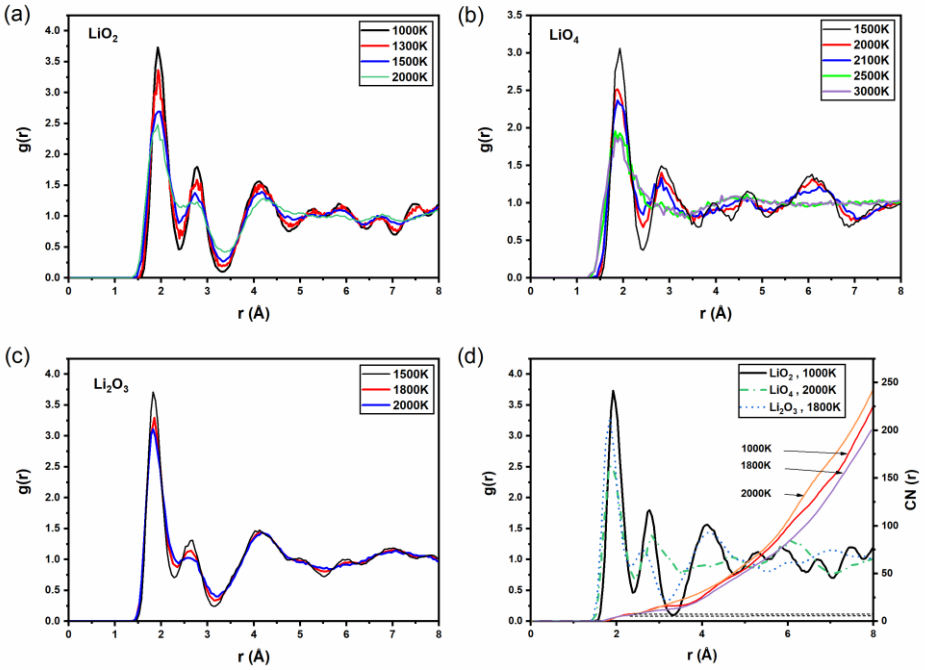

Fig. S3. The radial distribution function (RDF) and coordination number (CN) between Li atoms (central atoms) and O atoms (coordination atoms) at 1000-3000 K and 50 GPa for (a) LiO_2, (b) LiO_4, and (c) Li_2O_3. (d) The RDF and CN at a stable temperature. For LiO_2, the x-coordinate of the intersection between g(r) and CN(r) is 2.425 Å, and the CN is approximately 8. For LiO_4, the x-coordinate of the intersection between g(r) and CN(r) is 2.45 Å, and the CN is approximately 8. For Li_2O_3, the x-coordinate of the intersection between g(r) and CN(r) is 2.3 Å, and CN is approximately 6. These CNs are consistent with those in the primitive cell.

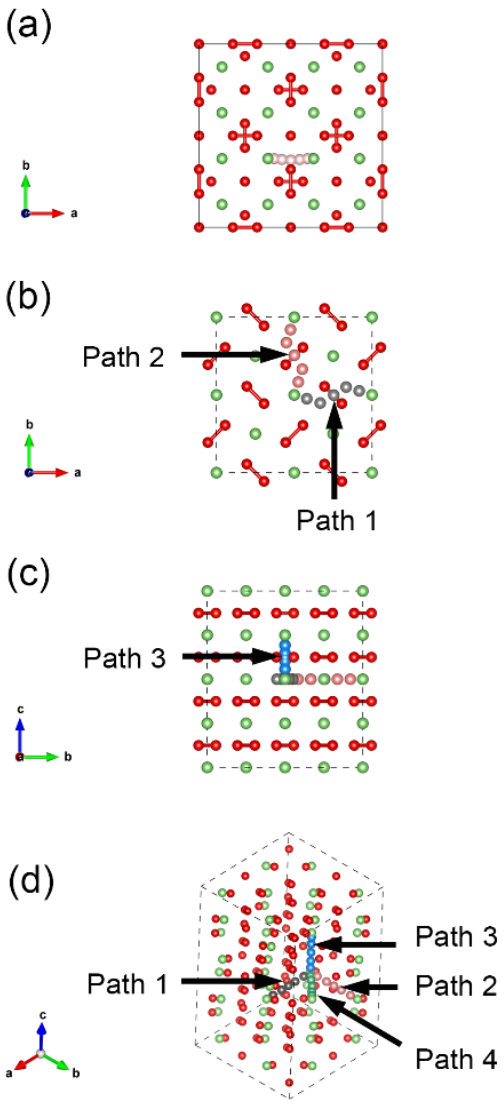

Fig. S4. The migration path of Li-O compounds. (a) Li_2O_3 along [100]. (b) The pink spheres represent the path of LiO_2 along [010], the black spheres represent the path of LiO_2 along [100]. (c) The blue spheres represent the path of LiO_2 along [001]. (d) The black, pink, blue and green spheres represent the path of LiO_4 along [100], [010], [001] and [110], respectively. Li and O are shown with light green and red spheres.